Hybrid Experimental Measurement of Sectional Stiffness Properties of the MERIT Rotor Blade with Digital Image Correlation

Tobias Pflumm* Lukas Gaugelhofer* Verena Heuschneider* Florian Berghammer*
Manfred Hajek†

Institute of Helicopter Technology
Technical University of Munich, 80333 Munich, Germany

A method to experimentally determine the sectional stiffness properties of modern fiber composite rotor blades is presented. This study hereby follows the novel approach introduced by Sinotte and Bauchau [1, 2]. The hybrid method relies on the measurement of the strain field and combines it with a numerically determined warping field. The strain field is measured using Digital Image Correlation (DIC)- a contact-free, optical 3D deformation measurement method in order to analyze and calculate deformations. The warping displacement field is recovered from a 2D cross-sectional structural analysis using the preprocessor SONATA and ANBA4. The design and manufacturing of the herein presented test article, the first rotor blade specifically developed for the Munich Experimental Rotor Investigation Testbed (MERIT) [3, 4], is described in detail and sectional stiffness properties are calculated based on the experimentally measured strains and loads.

Nomenclature

CAD	Computer-Aided Design
CI	Confidence Interval
C_{TW}	SGL - SIGRAPREG® C W200 TW2/2 E503/45%
C_{UD}	SGL - SIGRAPREG® U600-0/SD-E501/33%
DIC	Digital Image Correlation
FS	Rated Forces/Torque
MERIT	Munich Experimental Rotor Investigation Testbed
OL	Operating Limit
SD	Standard Deviation
VABS	Variational Asymptotic Beam Sectional Analysis
$\underline{\underline{A}}_{\mathcal{CG}}$	Transformation matrix
$\underline{\underline{A}}, \underline{\underline{B}}$	Strain interpolation matrices
$\underline{F}$	Sectional stress resultant
$\underline{\underline{K}}$	6×6 Cross-sectional stiffness matrix
$\underline{p}^G$	Position vector of the local coordinate system
$\underline{\underline{R}}_e$	Strain rotation matrix
$\underline{\underline{S}}$	6×6 Cross-sectional compliance matrix
$\underline{\underline{\mathcal{K}}}$	Curvature tensor
$\underline{\hat{u}}$	Nodal displacement
$\underline{\mathcal{U}}$	Average sectional displacement
$\underline{\underline{W}}$	Warping matrix under unit loads
$\underline{\underline{Z}}$	Nodal location matrix
$\underline{\varepsilon}$	Strain tensor
α_1	Spanwise coordinate
α_2, α_3	Cross-sectional coordinates

* Research Assistant, Corresponding Author: tobias.pflumm@tum.de

† Professor and Department Head, hajek@tum.de

Presented at 47th European Rotorcraft Forum, United Kingdom, 7-9th September, 2021

Introduction

State-of-the-art aeroelastic analysis tools such as CAMRAD II [5] or Dymore [6] calculate the blade-structural dynamics with one-dimensional (1D) beam elements. In comparison to fully resolved three-dimensional (3D) finite element models, this approach simplifies the mathematical formulation and increases the computational efficiency [7]. Therefore, knowing the spanwise distribution of the sectional stiffness properties is crucial for predicting the elastic and dynamic behavior of the rotor accurately. Typically, this approach decouples the realistic composite blade description from the aeromechanical analysis which is why over the past decades it has become state of the art to use a finite-element discretization of the cross-section for a linear two-dimensional (2D) analysis along with the 1D nonlinear beam analysis. Common tools are the Variational Asymptotic Beam Sectional Analysis (VABS) by Hodges and his coworkers [8], Sectionbuilder [9, 10] and ANBA4 [11, 12]. Their accuracy and efficiency has been validated in numerous publications [11, 13, 14].
Even though the structural description of the blades and predesign methods have improved in detail and accuracy, uncertainty still exists for the properties of the actual manufactured rotor blades. The problem is, that the rotor

system behavior can be very sensitive to modifications in some parameters. During the extensive studies of the HART I Rotor, the importance of accurate beam properties became evident as Jung and his coworkers [15] noticed poor agreement between predicted and measured structural loads in both magnitudes and phases. During later laboratory testing [16], they showed a discrepancy of up to 30% for the flap bending stiffness close to the inboard blade root section compared to the predesigned values.
The stiffness uncertainty can have numerous sources. The lack of knowledge or representation of the physics is described as epistemic uncertainty and can be reduced by improving prediction methods and the level of structural detail in the finite element discretization. The aleatory uncertainties are irreducible as they cannot be reduced through modeling techniques and are therefore rather a matter of production processes. For example, it has been reported that the coefficients of variation of the elastic moduli of a composite lamina can be 5 – 15% due to uncertainties associated with fiber and matrix material properties, fiber volume fractions, fiber orientation and undulation, intralaminar voids, etc. [17]. It was shown by the authors in previous studies [18], that the effect of material and manufacturing uncertainties can propagate through all levels of the aeromechanic simulation, resulting in substantial impacts on natural frequencies, elastic blade tip response and vibratory hub forces.

The objective of this work is therefore to further develop a method to experimentally determine the sectional stiffness properties of modern fiber composite rotor blades, which is a prerequisite for the prediction of dynamic behavior. The herein presented specimen of the methodology is the first rotor blade specifically developed for the Munich Experimental Rotor Investigation Testbed (MERIT) [3, 4], a rotor test bench designed for universal rotor and propeller aerodynamic and structural dynamic investigations, whose robust design allows for highly dynamic load applications such as Mach-scaled dynamic stall experiments.

The beam behavior is characterized by the symmetric 6×6 sectional stiffness matrix $\underline{\underline{K}}$ along the span leaving 21 desired properties for each radial station. This study hereby follows the novel approach introduced by Sinotte and Bauchau [1, 2]. While most classical experimental techniques rely on measuring the beam displacements or rotations using simplified beam models, neglecting coupling effects and averaging regions of interest, this hybrid method relies on the measurement of the strain field and combines it with a numerically determined warping field. The strain field is measured using Digital Image Correlation (DIC)- a contact-free, optical 3D deformation measurement method in order to analyze and calculate deformations. The surface structure of the specimen is recognized in digital camera images, and coordinates are assigned to image pixels. During the deformation of the specimen, images are taken and compared to the undeformed state in order to calculate the displacement and deformation of the object. In this case, the homogeneous surface of the rotor blade has few characteristic features, so the surface was pretreated with a stochastic color pattern.

Governing Equations

Based on the central solution of the nonlinear three-dimensional beam theory by Han and Bauchau [9, 10], the nodal displacement $\hat{\underline{u}}$ is described as the superposition of a rigid-section motion and the nodal warping introduced by sectional stress resultants $\underline{F}^T = \{F_x, F_y, F_z, M_x, M_y, M_z\}$.

$$\hat{\underline{u}}(\bar{\alpha}_1) = \underline{\underline{Z}}\underline{\mathcal{U}}(\alpha_1) + \underline{\underline{W}}\underline{F}(\alpha_1) \tag{1}$$

with

$$\underline{\underline{Z}} = \begin{bmatrix} \underline{\underline{z}} \\ \underline{\underline{0}} \end{bmatrix}; \quad \underline{\underline{z}} = \begin{bmatrix} 1 & 0 & 0 & 0 & \bar{\alpha}_3 & -\bar{\alpha}_2 \\ 0 & 1 & 0 & -\bar{\alpha}_3 & 0 & 0 \\ 0 & 0 & 1 & \bar{\alpha}_2 & 0 & 0 \end{bmatrix} \tag{2}$$

The first term of equation (1) describes the rigid-section motion at a specific point of the cross-section by multiplying the nodal location matrix $\underline{\underline{Z}}$ with the average sectional displacement $\underline{\mathcal{U}}$. The second term multiplies the nodal warping displacement under unit loads $\underline{\underline{W}}$ with the sectional stress resultant. The notation $\hat{(.)}$ indicates nodal quantities of the discretized model.
Assuming that the strain components remain small, the strain tensor $\underline{\varepsilon}^T = \{\varepsilon_{11}, 2\varepsilon_{12}, 2\varepsilon_{13}, \varepsilon_{22}, \varepsilon_{33}, 2\varepsilon_{23}\}$ is described by the following strain-displacement relation in matrix notation with the differential operators $\underline{\underline{A}}$ and $\underline{\underline{B}}$. $(.)'$ denotes the spatial derivative with respect to the spanwise variable α_1.

$$\begin{aligned} \varepsilon_{11} &= \frac{\partial u_1}{\partial \alpha_1}, & \varepsilon_{22} &= \frac{\partial u_2}{\partial \alpha_2}, & \varepsilon_{33} &= \frac{\partial u_3}{\partial \alpha_3}, \\ 2\varepsilon_{12} &= \frac{\partial u_1}{\partial \alpha_2} + \frac{\partial u_2}{\partial \alpha_1}, & 2\varepsilon_{13} &= \frac{\partial u_1}{\partial \alpha_3} + \frac{\partial u_3}{\partial \alpha_1}, & 2\varepsilon_{23} &= \frac{\partial u_2}{\partial \alpha_3} + \frac{\partial u_3}{\partial \alpha_2}, \end{aligned} \tag{3}$$

$$\underline{\varepsilon} = \underline{\underline{A}}\underline{u}' + \underline{\underline{B}}\underline{u} \tag{4}$$

By spatially differentiating the nodal displacement with respect to the spanwise coordinate $(\bar{\alpha}_1)$, the following equation is derived.

$$\hat{\underline{u}}'(\bar{\alpha}_1) = \frac{\partial \hat{\underline{u}}}{\alpha_1} = \underline{\underline{Z}}\underline{\mathcal{U}}'(\bar{\alpha}_1) + \underline{\underline{W}}\underline{F}'(\bar{\alpha}_1) \tag{5}$$

Together with the description of the sectional constitutive law $\underline{\varepsilon}_c = \underline{\mathcal{U}}'(\bar{\alpha}_1) + \underline{\mathcal{U}}(\bar{\alpha}_1) = \underline{\underline{S}}\underline{F}$ and the stress resultant equilibrium equation $\underline{F}' = \tilde{\mathcal{K}}^T\underline{F}$ with the 6×6 nondimensional curvature tensor of the undeformed beam $\tilde{\underline{\underline{\mathcal{K}}}}^*$, it can be introduced into equation (4) along with (1) giving the description of the three-dimensional strain tensor. Because

rigid-body displacements create no strains, the last term vanishes to zero.

$$\begin{aligned}\hat{\underline{\varepsilon}} &= \underline{\underline{A}}\underline{u}' + \underline{\underline{B}}\underline{u} \qquad (6)\\ &= \underline{\underline{A}}\left[\underline{\underline{Z}}\left(\underline{\underline{S}}\underline{F} - \tilde{\mathcal{K}}\underline{\mathcal{U}}\right) + \underline{\underline{W}}\tilde{\mathcal{K}}^T\underline{F}\right] + \underline{\underline{B}}\left[\underline{\underline{Z}}\underline{\mathcal{U}}(\bar{\alpha}_1) + \bar{\underline{\underline{W}}}\underline{F}(\bar{\alpha}_1)\right]\\ &= \left[\underline{\underline{A}}\left(\underline{\underline{Z}}\underline{\underline{S}} + \underline{\underline{W}}\tilde{\mathcal{K}}^T\right) + \underline{\underline{B}}\underline{\underline{W}}\right]\underline{F} + \underbrace{\left[\underline{\underline{B}}\underline{\underline{Z}} - \tilde{\mathcal{K}}\right]\underline{\mathcal{U}}}_{=0;\text{ rigid-body disp.}}\end{aligned}$$

$$\hat{\underline{\varepsilon}} = \left[\underline{\underline{A}}\left(\underline{\underline{Z}}\underline{\underline{S}} + \underline{\underline{W}}\tilde{\mathcal{K}}^T\right) + \underline{\underline{B}}\underline{\underline{W}}\right]\underline{F} \qquad (7)$$

Equation (7) provides the governing description of our problem. The inverse of the sectional compliance matrix $\underline{\underline{K}} = \underline{\underline{S}}^{-1}$ is the desired property. In our experimental setup, we can measure the sectional stress resultants $\underline{F}$ with a 6-axis load cell at the root-attachment of the blade and transform the loads to the desired spanwise location by using the free-body diagram. The second measured quantity are the plane surface strains $\varepsilon_{11,e}, \varepsilon_{12,e}$ and $\varepsilon_{22,e}$. The strains are always calculated in material, i.e. in local coordinates moving with the specimen while the e_3-axis is in the thickness direction. To ensure a common orientation of the strains, the strain rotation matrix $\underline{\underline{R}}_e$ is introduced to the equation. The full strain tensor can be derived with the knowledge of the material constitutive behavior but it is not needed, since the last three terms of the equation reduce to zero. The strain $\varepsilon_{13,e}$ is obtained through $\underline{\underline{R}}_e$ for values of $\theta \neq 0$.

$$\begin{aligned}\underline{\underline{R}}_e\hat{\underline{\varepsilon}}_e &= \left[\underline{\underline{A}}\left(\underline{\underline{Z}}\underline{\underline{S}} + \underline{\underline{W}}\tilde{\mathcal{K}}^T\right) + \underline{\underline{B}}\underline{\underline{W}}\right]\underline{F} \qquad (8)\\ \hat{\underline{\varepsilon}}_e &= \underline{\underline{R}}_e^{-1}\left[\underline{\underline{A}}\left(\underline{\underline{Z}}\underline{\underline{S}} + \underline{\underline{W}}\tilde{\mathcal{K}}^T\right) + \underline{\underline{B}}\underline{\underline{W}}\right]\underline{F}\end{aligned}$$

with the strain-rotation matrix defined as

$$\underline{\underline{R}}_e = \begin{bmatrix} 1 & 0 & 0 & 0 & 0 & 0\\ 0 & \cos\theta & \sin\theta & 0 & 0 & 0\\ 0 & -\sin\theta & \cos\theta & 0 & 0 & 0\\ 0 & 0 & 0 & \cos^2\theta & \sin^2\theta & \sin 2\theta\\ 0 & 0 & 0 & \sin^2\theta & \cos^2\theta & -\sin 2\theta\\ 0 & 0 & 0 & -\frac{1}{2}\sin 2\theta & \frac{1}{2}\sin 2\theta & \cos 2\theta \end{bmatrix} \qquad (9)$$

The hybrid approach is based on the fact that the warping displacement under unit loads $\underline{\underline{W}}$ is currently evaluated with the help of a sectional finite element model SONATA and ANBA4.

After mapping and interpolating the experimental strain data to the closest nodal location denoting $(.)_i$, at which the warping displacement is evaluated, the governing equation describes an overdetermined system of equations with independent load-cases denoted $(.)_j$.

$$\begin{aligned}\underline{\varepsilon}_{e,i}^{(j)} &= \underbrace{\underline{\underline{R}}_{e,i}^{-1}\underline{\underline{A}}_i\underline{\underline{Z}}_i\underline{\underline{S}}}_{\underline{\underline{U}}_i}\underline{F}^{(j)} + \underbrace{\underline{\underline{R}}_{e,i}^{-1}\left(\underline{\underline{A}}\underline{\underline{W}}\tilde{\mathcal{K}}^T + \underline{\underline{B}}\underline{\underline{W}}\right)}_{\underline{\underline{V}}_i}\underline{F}^{(j)} \qquad (10)\\ \underline{\varepsilon}_{e,i}^{(j)} &= \underline{\underline{U}}_i\underline{\underline{S}}\underline{F}^{(j)} + \underline{\underline{V}}_i\underline{F}^{(j)}\end{aligned}$$

The system is solved by using the half-vectorization of the symmetric compliance matrix leaving the 21 unknowns. The 6×21 matrix $\underline{\underline{G}}$ is defined with the duplication matrix $\underline{\underline{D}}_n\,\mathrm{vech}(\underline{\underline{S}}) = \mathrm{vec}(\underline{\underline{S}})$ as:

$$\underline{\underline{S}}\underline{F}^{(j)} = \underline{\underline{G}}^{(j)} \cdot \mathrm{vech}(\underline{\underline{S}}) = \underline{\underline{G}}^{(j)}\underline{S} \qquad (11)$$

$$\underline{\underline{G}}^{(j)} = \left(\underline{\underline{I}} \otimes \underline{F}^{(j)}\right)\underline{\underline{D}}_n \qquad (12)$$

$$\begin{aligned}\underline{\underline{U}}_i\underline{\underline{G}}^{(j)}\underline{S} &= \underline{\varepsilon}_{\varepsilon,i}^{(j)} - \underline{\underline{V}}_i\underline{F}^{(j)} \qquad (13)\\ \mathbb{A}\underline{S} &= \underline{b}\end{aligned}$$

The heavily over-determined system of linear equations is solved by minimizing the Euclidean 2-norm of $\|b - \mathbb{A}\underline{S}\|_2$. The sectional stiffness matrix $\underline{\underline{K}}$ is the inverse of the sectional compliance matrix $\underline{\underline{S}}$.

$$\underline{\underline{K}} = \underline{\underline{S}}^{-1} = \begin{bmatrix} k_{11} & k_{12} & k_{13} & k_{14} & k_{15} & k_{16}\\ k_{12} & k_{22} & k_{23} & k_{24} & k_{25} & k_{26}\\ k_{13} & k_{23} & k_{33} & k_{34} & k_{35} & k_{36}\\ k_{14} & k_{24} & k_{34} & k_{44} & k_{45} & k_{46}\\ k_{15} & k_{25} & k_{35} & k_{45} & k_{55} & k_{56}\\ k_{16} & k_{26} & k_{36} & k_{46} & k_{56} & k_{66} \end{bmatrix} \qquad (14)$$

Design and Manufacturing of MERIT Rotor Blades

The herein presented specimen of the methodology is the first rotor blade specifically developed for the Munich Experimental Rotor Investigation Testbed (MERIT) [4], a rotor test bench designed for universal rotor and propeller aerodynamic and structural dynamic investigations, whose robust design allows for highly dynamic load applications. One of the primary intended studies are Mach-scaled dynamic stall experiments.

As a baseline rotor for dynamic-stall experiments, the blades have no twist, a rectangular planform, NACA0012 airfoil, 130mm chord and a radius of 900mm. This simplicity allows an easier reproducibility and comparability with other experiments and numerical investigations. Many of these requirements have been defined by MERIT and its intended purpose. The hub of the MERIT test bench illustrated in figure 1 is a hingeless design: The blade clamps (1) have a preset pitch of 10° and are supported by two needle bearings each (4) to allow for pitch changes on each blade, while the flap and lead-lag motion is mainly accommodated by the blade's elastic behavior. The pitch links are attached at (2) to the blade clamps. Torsionally soft sheet metal tension torsion straps (3) transfer the high centrifugal loads to the centerpiece (5). The relatively stiff hub design gives the test-bench a powerful response to control inputs and reduced blade movements.

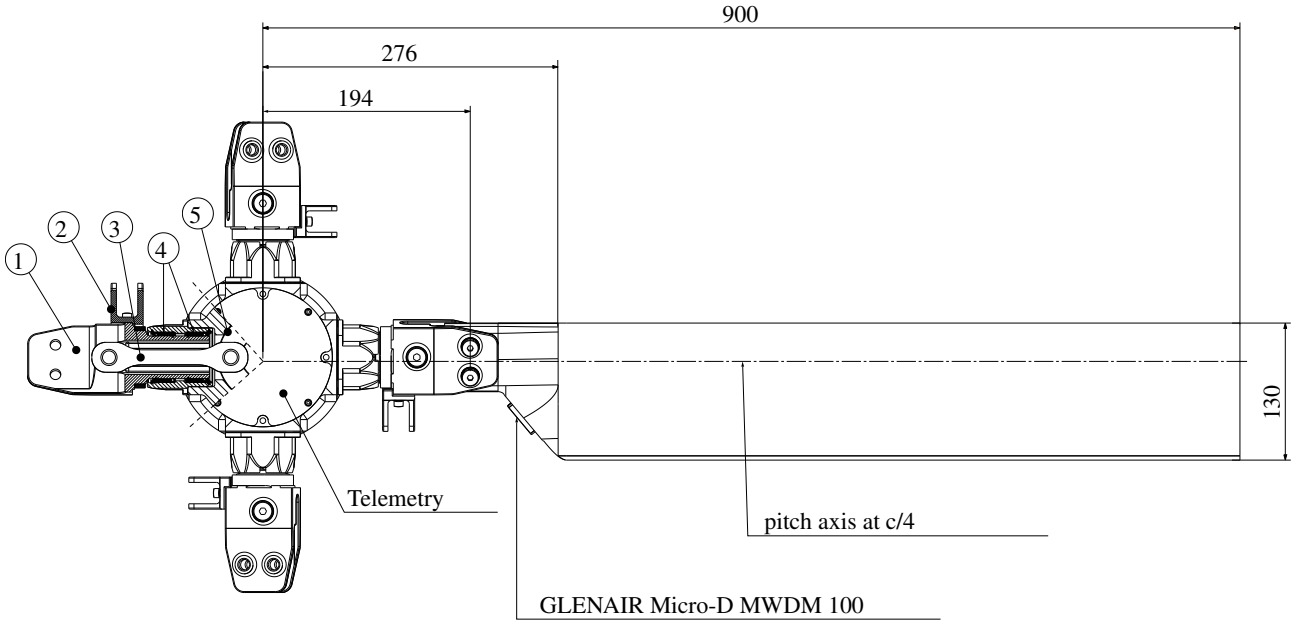

Fig. 1: MERIT rotor hub and blade dimensions

Blade Attachment

The blade attachment is designed as a bearing laminate. In this case, no loops are wrapped around a bolt, but a simple ply pack is stacked on top of each other, into which bushings are subsequently drilled. In this case, the laminate and the bolt connection must be designed for bearing laminate failure. This type of failure can be described as good-natured, since the hole merely deforms and does not fail abruptly as separation. It occurs slowly, since the fiber composite redistributes stress peaks through interfiber fractures and delamination. The failure announces itself in time [19–22].
Important parameters for the strength of the blade attachment are the distances of the holes to the sides of the laminate. The dimensions shown in figure 2 are decisive for the subsequent strength of the connection. The attachment is

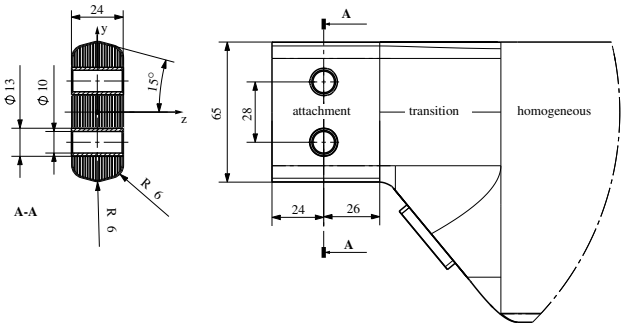

Fig. 2: blade attachment and layup cross-section at R194

designed around two high strength steel bolts with a diameter of ∅10 mm, while ∅13 mm glued-in bushings guide the bolts. This is to prevent damage to the holes in the laminate due to frequent assembly. A glued-in bushing also smoothes out the surface pressure. In addition, the adhesive heals the microscopic interfiber fractures produced during drilling, while sealing it against moisture penetration and insulating it to prevent contact corrosion between the metallic connecting elements and the fiber composite.
The bushings are made of aerospace grade Böhler N352 stainless steel, a martensitic chromium steel with nickel addition, resistant to the effects of seawater and acids [23].
The blade attachment has a thickness of 24 mm. A lateral inclination of 15° ensures better demoldability, while the radii of the cross-section provide better drapability during the manufacturing process.

The following layer thickness ratios are realized for this laminate: 50% fraction of 0° layers, 45% fraction of ±45°-layers and 5% fraction of 90° layers [20]. The ply structure is symmetrical to prevent undesirable normal force, bending or torsional couplings. In addition, the differences in fiber angle between adjacent plies is designed as small as possible, as this reduces the interlaminar shear stresses in the laminate. It should also be noted that only a maximum of three plies are adjacent to each other in the same fiber direction. This reduces crack growth in the matrix of the fiber composite and thus increases the damage tolerance of the laminate. Other requirements for the laminate include that the adjacent plies differ by less than 60°, as this reduces interlaminar stresses and residual stresses during the curing process.
Since the blade attachment has the thickest laminate, and the ply structure in the rotor blade changes over the radius, the plies in the transition area must be scarfed. This also results in further important requirements for the blade and laminate design that must be taken into account.

Two different composite materials are used for the blade. The first composite material (SGL Carbon -

SIGRAPREG® U600-0/SD-E501/33% (C_{UD})) is an UD epoxy/carbon fiber prepreg with a fiber areal weight of 600 g/m^2. This material combines a HT carbon fiber with a epoxy resin (E501) with 33% weight fraction, designed for low curing temperatures of 80°C - 160°C with relatively short curing times. This makes this prepreg system particularly suitable for applications where only low temperatures are possible for curing [24]. For our application a low curing temperature is crucial to reduce thermal stresses and to protect the metrology that can be integrated into the blade structure before curing.
The second material (SGL Carbon - SIGRAPREG® C W200 TW2/2 E503/45% (C_{TW})) combines the same epoxy resin (fractional weight of 45%) with a 200 g/m^2 2x2 twill weave HT carbon fiber [25]. The twill weave is chosen for its improved drapability and reduced fiber undulation compared to a plain weave.
After consultation with the material supplier, both materials are considered to be the exact same as it was used for the design and manufacturing of the AREA rotorblades [26, 27]. Although there are materials with superior strength characteristics, this material was selected for the MERIT rotor blades based on existing experience with handling, curing cycles and the experimentally characterized constitutive behavior [28].

The first three layers compose the blade skin (sk) that stretch over the entire blade and which is mainly responsible for the torsional stiffness, which is why the twill-fabric C_{TW} is used here at $\pm 45^\circ$ to the longitudinal axis of the blade. This allows the fibers to be aligned along the principal stresses under torsion [19]. As the exterior part of the structure, the thinner woven fabric has a high impact resistance to be robust enough to withstand minor accidental impacts during handling and ensures a high surface quality. To increase the electromagnetic compatibility (EMC) of integrated metrology, Aaronia-Shield® [29], a high performance silver/polyamide blend (20%/80%) net with a very low areal weight, can be placed optionally in between sk1 and sk2.

The unidirectional layers for the spar (sp) range from the attachment to the tip of the blade. The spar plies are evenly distributed in the blade attachment area and have several layers of C_{TW} fabric separating them as transition (tr) plies. The transition plies are scarfed and disappear in the homogeneous section of the blade.

The strength margins for the blade attachment under operational loads are predetermined based on an experimental bearing laminates study with the same material and proportion of plies [21, 30] and later verified during a destructive blade tensile test [3].

Homogeneous Section

The homogeneous blade area is the aerodynamically effective area that provides the necessary lift and thrust. It ranges from R276 to the tip at R900 with a NACA-0012 airfoil. The airfoil was selected because it is a frequent test case in computational fluid dynamics and a good reference to start with. In figure 3 the airfoil and the cross-sections of the homogeneous section is illustrated. The cross-section consists essentially of the skin, spar, core, trim weight, and a trailing edge tab. One of the most important requirements for the cross-section is that the center of gravity is at 25% chord to keep control and torsional forces low and avoid aeroelastic instabilities.

Due to a two-part manufacturing process, a trailing edge tab not only increases the shear stiffness between the two halves of the skin, but also considerably simplifies the manufacturing process creating a secure bond of the blade. An enlarged section of the trailing edge is shown in figure 3 in detail B. The thickness of the tab of 1.44 mm corresponds to six times the thickness of the C_{TW} fabric. The tab is intersected with the original NACA 0012 airfoil and rounded with a radius of 2 mm.

The cross-section shown in figure 3 has a C-shaped spar construction. The spar carries primarily the flapping and lead-lag bending moments as well as the centrifugal forces and is made of C_{UD} in the direction of the blade's axis. The advantage of the C-shaped spar is that the center of gravity as well as the shear center are located at the front of the cross section [19] while the manufacturing remains simple. The layup is summarized in table 1.

seq.	name	material	orientation	thickness
1	sk1	C_{TW}	$\pm$ 45°	0.24
2	emc	Aaronia-Shield	0°	0.10
3	sk2	C_{TW}	$\pm$ 45°	0.24
4	sk3	C_{TW}	$\pm$ 45°	0.24
5	sp1	C_{UD}	0°	0.56
9	sp2	C_{UD}	0°	0.56
13	sp3	C_{UD}	0°	0.56
17	sp4	C_{UD}	0°	0.56
21	sp5	C_{UD}	0°	0.56
24	sp6	C_{UD}	0°	0.56
28	sp7	C_{UD}	0°	0.56
32	sp8	C_{UD}	0°	0.56
36	sp9	C_{UD}	0°	0.56
- - - - - - - - - - - - **symmetry plane** - - - - - - - - - - - -				

Table 1: layup of the homogeneous section: skin (sk), spar (sp)

To move the center of gravity of the cross-section forward, a balance weight is used near the leading edge. For this purpose a ∅ 5 mm Pb97Sb3 trim mass is integrated after the first two spar layers, to give more space for pressure sensors and other metrology to be integrated near the leading edge of the blade. The alloy was used as antimony increases the mechanical properties compared to pure lead. The material's low modulus of elasticity and sufficient elongation at break makes it insensitive to the blade movements and deformations that occur during

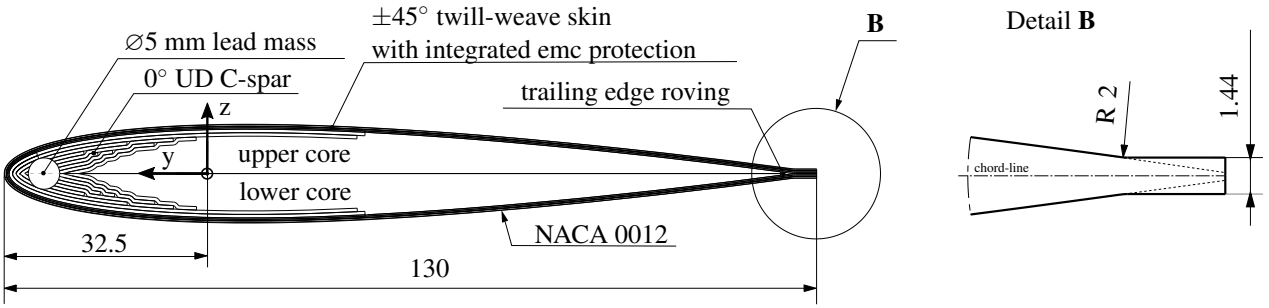

Fig. 3: homogeneous section composite layup with a NACA-0012 airfoil with modified tab

operation.

The largest component of the homogeneous section is the *Rohacell® 51 RIMA* low density filler material, a closed-cell polymethacrylimide (PMI) rigid foam specially designed to ensure a minimum uptake of resin that is dimensional stable up to temperatures of 200 °C [31].
During the manufacturing process, this core has the task of positioning the uncured components of the rotor blade and is responsible for applying the necessary pressure to the laminate during curing. Therefore, a certain pressing oversize should be taken into account in the design of the core [22]. In the cured state, the core ensures on the one hand the stability of the skin to prevent buckling, and on the other hand it protects the skin against further damage caused by punctual pressure loads [19]. In order for the cross-section to remain stable under torsion, the core is compression resistant.
The core is machined into two parts in order to create the possibility to integrate the cables for measurement equipment and to route them between the cores near the neutral axis of the cross-section.

At the trailing edge, a good bond between the two halves is provided by the tab. Nevertheless, an additional trailing edge roving is inserted between the core and the tab to prevent the skin from collapsing during curing.

Transition Region

The section exposed to the highest loads and strains which defines and ensures the dynamic and flight mechanical properties of the rotor is the transition region. Therefore, special attention is paid to the bending stiffnesses and strains of the laminate during sizing.
When designing the outer geometry of the transition area, special care is taken to create a smooth and fluid transition. Edges and corners are avoided in order to obtain a shape that is suitable for a force-flow-compatible design including a careful scarfing of the laminate. Thickness changes are gradual in order to avoid stress concentrations in the laminate while attention is paid to the symmetry of the residual laminate [26]. Figure 2 and 4 shows the transition area of the rotor blade.

An aerodynamically favorable shape is created by large radii at the leading edge and a trailing edge that is pronounced towards the end. The trailing edge tab is extrapolated from the homogeneous area to the transition area.
A significant aspect is the integration of a Glenair® Micro-D connector that can be specified with either 100 electrical pins or up to 8 fiber optical termini. Stainless steel blind rivet nuts with threadsize M3 are riveted into the holes of the connector. An attached thin aluminum retainer sheet thereby provides an additional form-fit of the connector assembly with the cured laminate.

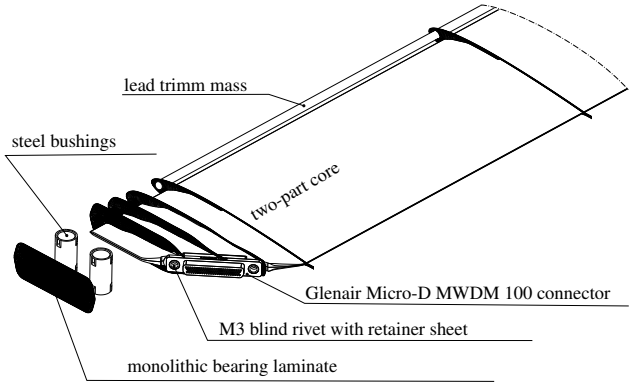

Fig. 4: 3D section view of the composite layup

Balance Chamber

Each rotor blade and the rotor head itself are subject to certain manufacturing tolerances. These lead to differences in blade weight and center of gravity position and mass distribution of each blade, so that the overall center of gravity of the rotor also has a small radial distance from the axis of rotation. With a rotor diameter of ∅ 1.80 m, the MERIT test rig has small dimensions, but is to be operated at blade tip speeds of up to 220 m/s. The resulting high rotational speeds imply very low unbalance tolerances.
To compensate for the unbalance, a balancing cell is installed on the pitch axis, at the blade tip of each rotor blade, as shown in figure 5. It can be filled with balancing weights made of brass and tungsten, which are pressed

against tapped grub screw by a compression spring. The chamber itself is machined out of titanium and is glued with the help of adhesive grooves into the quasi-isotropic monolithic structure of the blade tip. The volume is large enough to change the static moment of the blade by about 2% [32]. To prevent loosening of the screw due to vibration a stainless steel HELICOIL® Plus Screwlock thread insert is used in combination with a threadlocking adhesive. The balance cell is sealed with a movement detection paint to enable a visual inspection of a possible loosening. This simple design solution features a flat rotor blade end.

The blades are initially statically balanced on a 3-axis force/torque sensor (K3R70 20N/0,2Nm by ME-Messsysteme) which is mounted between a base plate and an adapter plate to attach the rotor blades. The performance and achievable measurement accuracy of 20 gmm was verified in various test series.
The measurement crosstalk between the axis $M_{x,0}(F_z)$, $M_{y,0}(F_z)$ was calibrated with the use of machined discs of different weight. Both $M_{x,0}(F_z)$ and $M_{y,0}(F_z)$ were found to be linear functions passing through the origin with which the zero-point offset is compensated.

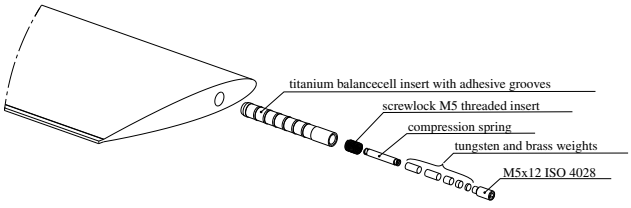

Fig. 5: exploded view of the balance chamber

Manufacturing

Manufacturing the rotor blades is a two stage process that allows the integration of metrology onto cured lower and upper shells and can be reduced to a single stage press molding process. The first stage cures the skin and two spar layers in an autoclave curing process leaving shells to be instrumented. During the second stage the remaining layup with all components is cured by compressing the warmed up molds and laminate.
The mold was designed to meet the requirements of both an autoclave vacuum process and press molding. Its functional design is illustrated in figure 7 and is briefly described below:

Mold Design The mold consists of a mold top and a bottom machined out of an EN AW 7021 precision cast aluminum plate with high dimensional stability and low residual stresses. A rip structure creates a stiff but lightweight design that offers good heat transfer during oven heating while at the same time enables easy handling.
Because vacuum bags are regularly applied for the first cure

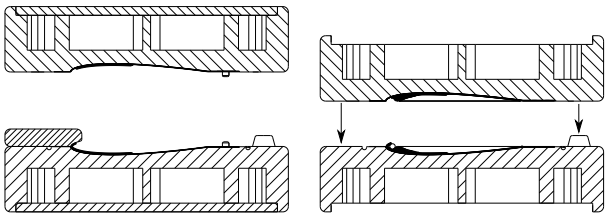

(a) Cure Cycle 1: vacuum autoclave **(b)** Cure Cycle 2: press moulding

Fig. 6:

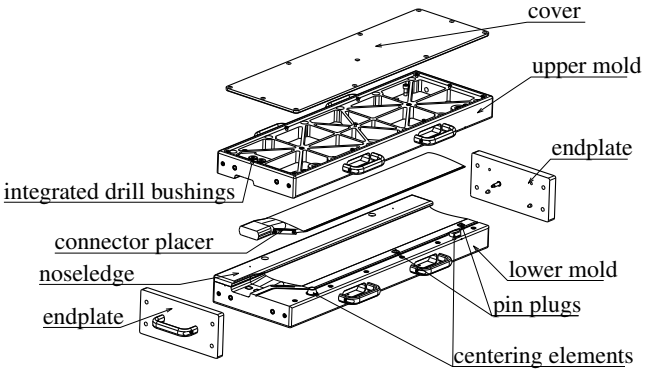

Fig. 7: mold assembly

cycle in the autoclave and vacuum compacting the thick layup, round edges are all around to prevent ruptures of the bagging as a lid is covering the rip structure. A noseledge is attached during the first curing cycle to create an overlap of the lower and upper shell at the leading edge.
The manufacturing edge is extended at the leading and trailing edge, at the tip and at the blade attachment allowing a homogeneous laminate. The excess material at the trailing edge allows to integrate two centering holes into the cured shells for further positioning by placing removable pin plugs into the mold. Scribelines indicate the final edge of part. At the blade attachment similar centering spike plugs are used leaving a centering bore in the blade that assists the precise position of the hole during drilling. Note that the molds also function as drilling jig after the blade is cured using integrated drill bushings that lay beneath the removable spike plugs.
Twelve high strength M10 screws compress the two halves, while a conical and a half-cylindrical centering element ensures precise positioning. The connector placer helps to position the connector during the process. End plates close the mold at both ends of the mold while a channel traps excess resin. Thermocouples can be placed just underneath the surface of the part to monitor the temperature during curing in the middle, at the blade attachment and at the tip. To obtain a high surface quality, the mold was sanded and polished before sealing it and applying release agent.

Cure Cycle 1 First, the serial number *S/N: MERIT-A-001-2020-07* (A: revision, 001: sequential number, 2020-07: manufacturing year and month) is placed into the upper mold.
The skin plies and the optional emc-protection are then

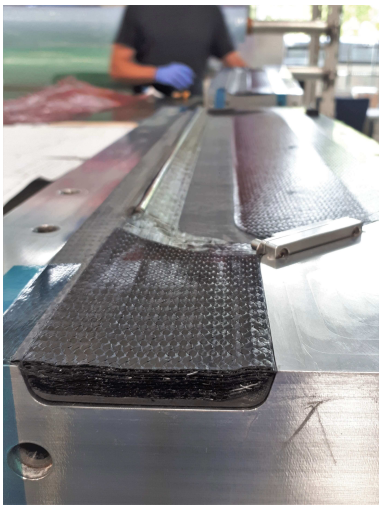

(a) monolithic blade attachment

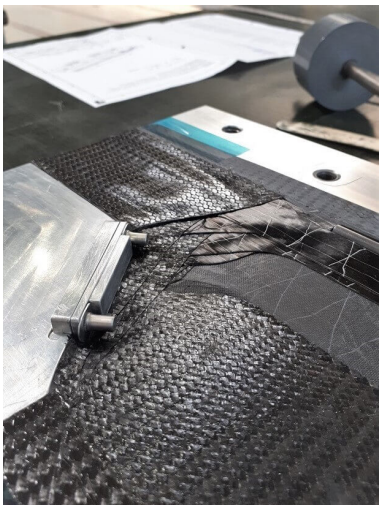

(b) scarfed transition with connector dummy

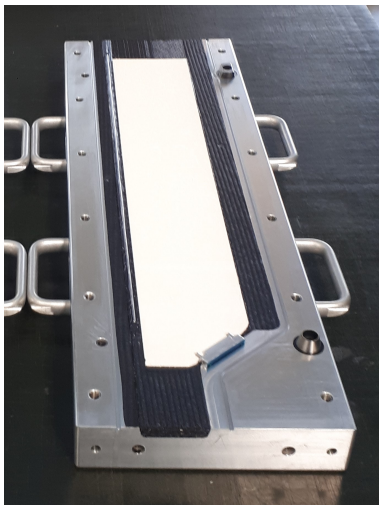

(c) foam core placed in the lower mold

Fig. 8:

placed into the molds. Note that the third skin layer (sk3) is split into a front and aft part, while the latter being applied during the second cycle to ensure a solid bond of the trailing edge tab. The layup for the first cycle is completed with the first two spar layers (sp1, sp2) and the first transition plies. This shell thickness provides enough space for the later integration of pressure sensors. The stack-up is completed by covering it with peel ply, perforated release film and breather fabric before sealing it into a vacuum bag. The shells are cured under vacuum condition (minimum of -0.7 bar) at 90°C (with a 1°C/min heat-up rate) at 4 bar autoclave pressure for 6 hours.

Cure Cycle 2 In preparation of the second cycle, excess material, particularly at the leading edge overlap, is removed and both shells are matched to each other. At this point metrology can be installed onto the shells, which is not described as part of this work. A dummy replaces either the electrical *Glenair® MWDM 2L-100p-6e5-18* Micro-D or the fiber optical Micro-D connector if the blades are not instrumented. The connector is placed into the connector-placer and sealed against an unwanted resin entry.
The thoroughly cleaned shells are placed into the molds and the remaining plies are stacked on top of each other. Note that besides the blade root, the tip consists of a quasi-isotropic monolithic section with alternating $\pm 45°$, $0/90°$ C_{TW} plies.
Once all layers are laid, the trim mass is carefully placed in the groove of the spar layers and the space to the leading edge is filled by a C_{UD} roving. As seen in figure 8, the final step before closing the halves is the placement of the milled foam core halves, which were previously covered with SGL CARBBON - SIGRAPREG® F 147-E322/100% epoxy film-adhesive. The aforementioned trailing edge roving is subsequently placed and the connector is placed between the core halves in the recess.

The cure cycle has an initial heating ramp-rate of 1°C/min from room temperature to 80°C that is maintained for 4h. The mold halves are compressed once the monitored thermocouple temperature reaches 77°C. After the first ramp the temperature is increased to 100°C at 1°C/min with a dwell of 8h.

Experimental Setup

As described through the governing equations, the plane surface strains $(\varepsilon_{11,e}, \varepsilon_{12,e}, \varepsilon_{22,e})$ and their corresponding cross-sectional coordinates need to be determined under at least six precisely known linearly independent load cases $(F_x, F_y, F_z, M_x, M_y, M_z)$ at three or more points of the cross-section. To determine the sectional stiffness properties along the span, this measurement needs to be repeated at multiple cross-sections. By measuring the forces and moments at the blade root as the loads are applied at the tip, it is possible to calculate the forces and moments acting in every blade sections using a free-body diagram. To account for geometric non-linearities the deformation of the blade needs to be measured as well.

The test stand shown in figure 9 was specially built for this purpose [33]. It uses the sturdy steel frame, previously used for rotor blade investigations by Hajek et. al. [34] and Suesse [27].
The blade is mounted with two ⌀10 mm bolts vertically onto a 6-axis load cell with an adapter that has the same geometry and material as the original MERIT blade clamps. The load cell itself is in turn attached to a base plate that is screwed to aluminum flat sections on the floor.
All loads are applied at the tip of the blade via steel cables and a system of pulleys. Aluminum profiles are used to equip the steel-frame with modular components that allow to vary the mounting position of cable pulleys. The

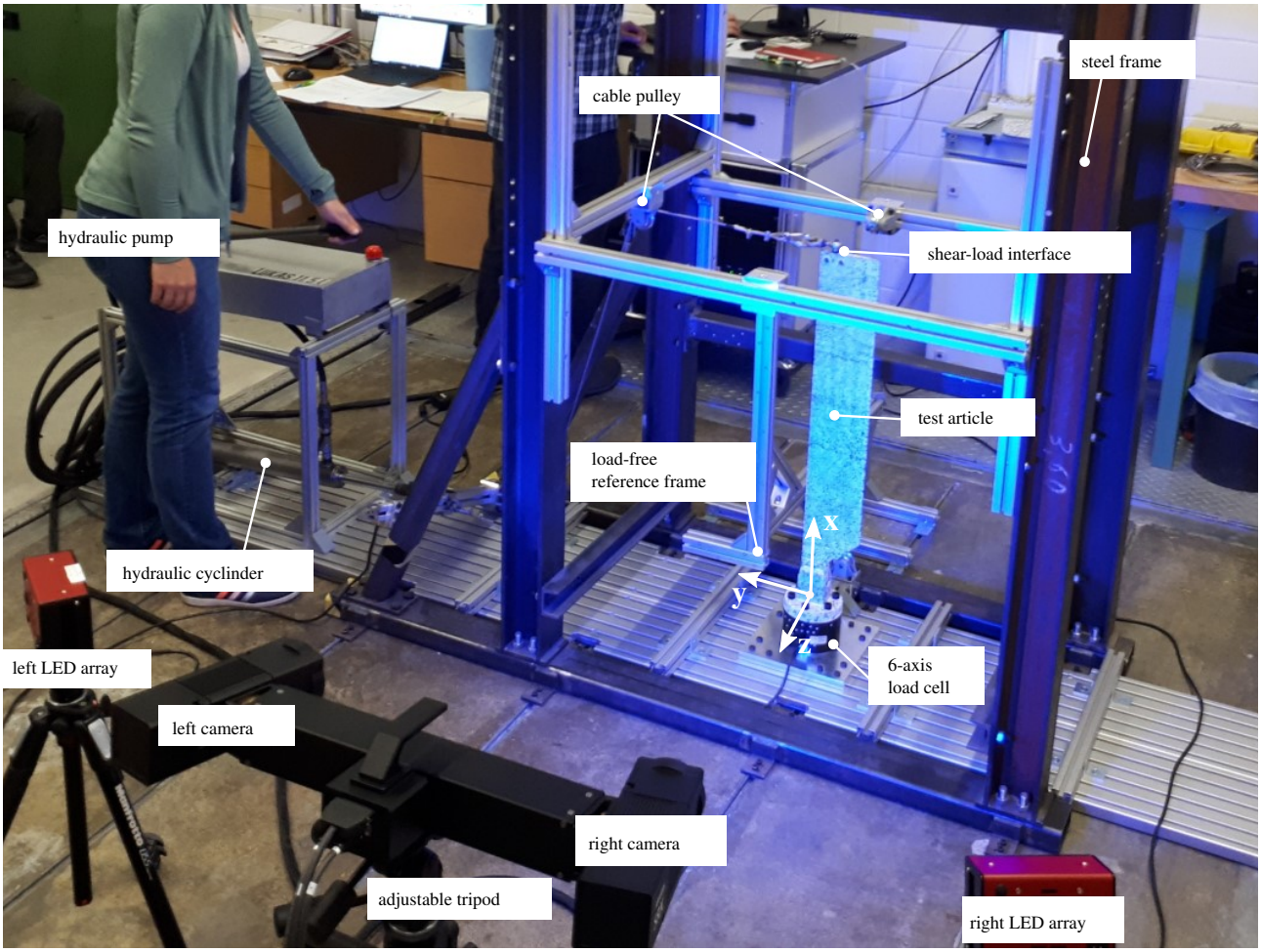

Fig. 9: experimental setup: testbench for load application and DIC system measurement setup.

force is introduced via a hydraulic cylinder in combination with a hand actuated hydraulic pump. The advantages are large forces, simple equipment, great damping characteristics and precise load repeatability.

Load Application

It is important to highlight that the experiments are non-destructive, which means that neither the applied loads exceed the strength capacity of the blade structure nor that the load-interface at the tip of the blade prevents further usage. The blades are manufactured with the quasi-isotropic monolithic tip layup extending 34 mm over the finished engineering edge of part that is used for a tough load-interface by inserting a cylindrical steel pin at the pitch axis at 25% chord and two steel bushings.

In figure 10 the experimental setup of the load cases are shown. Considering the coordinate system of the blade, F_x is the axial force along the longitudinal axis, F_y is the transverse force in lead-lag direction and F_z in flap direction. Analog, the torsional moment about the longitudinal pitch axis is denoted M_x, the bending moment in flap direction M_y and M_z in lead-lag direction. All loads are applied in positive and negative direction, except for the negative axial force due to the potential risk of buckling, leaving 11 load-cases shown in figure 10.

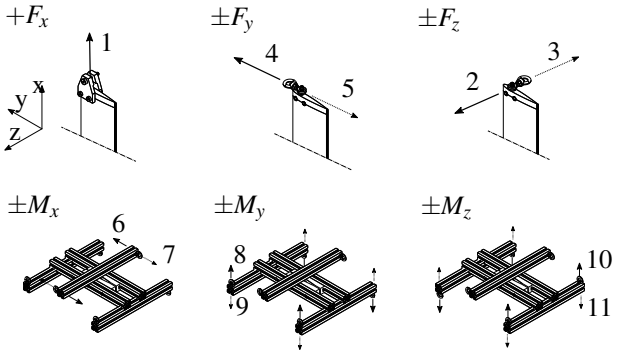

Fig. 10: independent load cases in positive (solid) and negative (dashed) direction, the index indicates the corresponding test case.

For the axial load case, the two integrated bushings are used to connect a steel cable via an adapter as shown in

figure 10. This allows coupling relations of the stiffness-matrix to become more visible during the experiment as the movement in the other directions is less counteracted. Due to the load capacity of the pulleys the axial load was limited to 10 kN.

To reduce undesired forces and moments, the transverse forces F_y (4, 5) and F_z (2, 3) are applied precisely at the pitch axis with the help of the glued-in cylindrical pin via a spherical rod end. A ring nut transfers the applied forces of the hydraulic cylinder from the steel cable to the rod end. Note that, depending on the spanwise position, the transverse forces at the tip induce a sectional bending moment.
A force couple of equal and opposite magnitude is introduced to a frame that transfers the torsional moment M_x (6, 7) via blade clamps onto the blade. The clamps are secured with two cylindrical pins through the blade bushings to prevent undesired movement. To ensure equal force magnitudes the steel cable is routed back through pulleys at the hydraulic cylinder.
The bending moments M_y (8, 9) and M_z (10, 11) are applied with the same load frame. However, four forces instead of two are now applied with the same magnitude and opposite direction at the outer corners to provide a free image area in front of the blade surface. Again, to ensure equal force magnitudes the steel cable is routed back through pulleys at the hydraulic cylinder which are attached at a hinged bar.

Load Cell

Accurate measurements of the applied loads are the basis of the described method. The 6-axis multi-component sensors (*K6D130 5kN/500Nm MP11* by *ME-Meßsysteme GmbH* [35]) for forces and moments $\underline{F}^T = \{F_x, F_y, F_z, M_x, M_y, M_z\}$ was specifically selected for the desired operating range to obtain the best compromise between maximum load capacity and measuring accuracy. To obtain a high signal to noise ratio of the strain measurements, the target loads are calculated with the structural model of SONATA for a corresponding target strain estimate of $\sim 0.3\%$. The nominal forces and moments (full scale (FS)) of the load cell are provided in table 2.
Sinotte [2] stated that the hardest part of getting good measurements with their test setup was obtaining accurate measurements of the applied loads, which is why they performed an elaborate calibration and uncertainty study to reduce the errors in the load measurements.
In this case, the calibration was carried out under consideration of DIN EN ISO/IEC 17025 by the manufacturer. With a probability of 95%, the measurement results have the uncertainties listed in table 2. More measures of precision and crosstalk are given by the manufacturer.

Technica Data *K6D130 5kN/500Nm MP11*			
Channel	FS	95% CI	OL
F_x [kN]	15	$\pm$31.5	45
F_y [kN]	5	$\pm$4	15
F_z [kN]	5	$\pm$12	15
M_x [Nm]	500	$\pm$0.5	1500
M_y [Nm]	500	$\pm$0.6	1000
M_z [Nm]	500	$\pm$0.65	1000

Table 2: Technical Datasheet of the *K6D130 5kN/500Nm MP11* Load Cell by *ME-Meßsysteme GmbH* [35], [36]. Rated Forces/Torque (FS), Confidence Interval (CI), Operating Limit(OL)

DIC Setup

To fill the remaining components of the governing equation (10), the plane surface strains $(\varepsilon_{11,e}, \varepsilon_{12,e}, \varepsilon_{22,e})$ and their corresponding cross-sectional coordinates $(\underline{Z}_i)$ and orientation $\underline{\underline{R}}_e$ are determined using Digital Image Correlation (DIC).
Sinotte and Bauchau [1, 2] generated a high local resolution by subdividing their specimens into multiple spanwise images and later reassembled them, yet used a high spatial filter size to smoothen the data afterwards. In contrast to that, it was decided to use a camera setup and measurement volume that can capture the full surface of the blade, the blade clamp, load cell and a load-free reference frame for a rigid-body motion correction.
An ARAMIS SRX 600 MV1200 sensor by *GOM* was used to capture images for full-field and point-based measurements with a resulting calibrated field of view of 920 mm $\times$ 1140 mm $\times$ 920 mm with an image size of 4096 $\times$ 3068 pixels leaving enough in depth space for large deflections under flap bending loads. The two stereo-cameras with a focal length of 24 mm are oriented 25.533° inwards to obtain 3D measurements. The sensor needs to reach its operating temperature in order to achieve thermal equilibrium. Otherwise thermal expansion of the beam, camera sensor or lenses can cause a drift in the intersection deviation. Additional LED arrays provided a homogeneous illumination of the test articles.

Sample Preparation

Three to four layers of matte white 2-component epoxy resin-based primer were applied to generate a smooth white primary coat before applying the matte black stochastic pattern with a brushlike sponge. (see figure 11a) The ideal pattern size and distribution was determined prior to the experiments by evaluating various pattern samples on paper by the DIC Software in the test configuration.

Figure 11b shows the prepared test articles in the test configuration. Figure 11c shows the 50 mm$\times$50 mm cutout of the pattern illustrating a resolution of approximately $\sim$3px/mm on the test article.

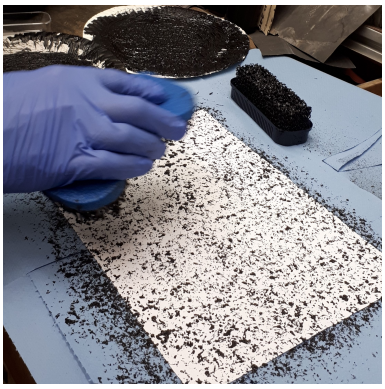

(a) speckle patter application with a soft plastic sponge

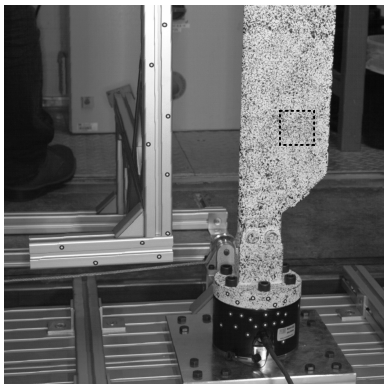

(b) prepared test articles

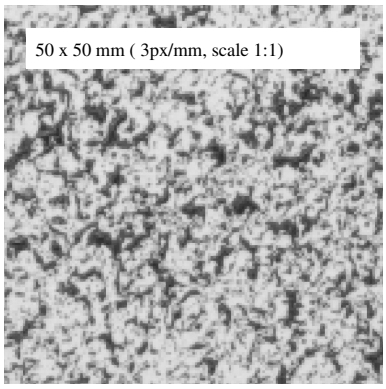

(c) true to scale cutout of the speckle pattern

Fig. 11:

∅5 mm reference point markers are distributed on the load-free reference frame, the cylindrical surface of the blade clamp, and the surface of the load cell. Additionally, a touch probe with reference point markers permitted to make 3D-point measurements of hidden areas such as the full cylindrical surfaces or flat plane of blade clamp. The capture of these distinct geometric objects allows the reference of a coordinate system.

Test Envelope

The tests were conducted by applying the previously described 11 load cases. The load amplitudes were selected based on preliminary structural calculations to achieve a targeted maximum strain of about 0.3% to ensure a high signal to noise ratio, but at the same time leaving safety margins. For most load cases, the load was applied in three amplitude steps. The test envelope of the highest loads levels is summarized in table 3.

Again, a negative axial load $-F_x$ was not applied due to concerns about buckling.

All experiments were conducted for the upper and the lower surface of the rotor blade by rotating the base plate together with the load cell and the blade by 180°. The test number listed here refers to the surface, load case and load level (e.g L6.3; L:lower surface, 6: +torsion, 3:3rd load application step).

Independent load cases were targeted by reducing the off-diagonal terms of the test envelope table. Additionally, it was targeted to match the load cases of both sides.

For each test, 20 images were taken with a frequency of 2 Hz to offer the possibility to average the data over time.

		Measured Maximum Loads					
Load Case	Test #	F_x [N]	F_y [N]	F_z [N]	M_x [Nm]	M_y [Nm]	M_z [Nm]
Axial, F_x	L1.2	**10045**	-198	-4	0.7	-3.2	-104.9
	U1.2	**10040**	-83	-78	0.3	22.8	-24.5
Lag Shear, F_y	L2.2	79	**659**	-50	-0.3	-1.5	597.2
	U2.2	159	**659**	-44	0.0	0.1	604.4
	L3.2	66	**-734**	-20	0.7	-2.7	-673.2
	U3.2	139	**-735**	-44	1.3	-0.6	-672.9
Flap Shear, F_z	L4.3	40	-13	**-502**	-1.1	458.2	-7.3
	U4.3	49	-11	**-501**	-0.4	440.1	-2.0
	L5.3	63	6	**504**	0.9	-461.5	0.7
	U5.3	55	16	**503**	0.5	-455.3	7.8
Torsion, M_x	L6.3	-74	11	-51	**179.8**	33.4	2.8
	U6.3	-66	22	-17	**179.5**	-2.4	15.1
	L7.3	-67	-5	-16	**-123.8**	4.7	-2.2
	U7.3	-68	4	-14	**-123.6**	-2.8	5.4
Flap Bending, M_y	L8.3	-43	-29	30	-4.6	**300.3**	-28.9
	U8.3	-123	-12	-38	0.3	**300.3**	-2.6
	L9.3	-22	-27	-68	1.7	**-301.0**	-27.9
	U9.3	-186	-9	-42	2.1	**-301.5**	-5.0
Lag Bending, M_z	L10.3	-63	-42	-53	1.7	8.5	**469.8**
	U10.3	-143	-79	-34	0.9	-1.7	**470.7**
	L11.3	-88	0	-24	2.1	-4.3	**-604.8**
	U11.3	-165	-39	-28	2.5	-9.6	**-606.3**

Table 3: test envelope of the measured loads at the load cell, Test # refers to the (L:lower, U:upper) surface.

Postprocessing

The momentary capture of the combined set of stereo images and analog signals from the load cell is hereinafter referred to as stage. All stages are further processed with the DIC software *GOM Correlate Professional 2020*.

For the initial alignment of the measurement data with respect to a coordinate system, the cylindrical and the plane surfaces of the blade clamp are used that were previously captured with the 3D touch probe.

When generating the so called surface-component, the software identifies facets in all captured images using the stochastic pattern structure and identifies all facets of the left camera image in the stochastic pattern of the right camera image. The software merges all calculated measuring points from valid facets into one surface-component. The surface-component with a facet size of 23 px and a facet spacing of 11 px covers almost the entire visible surface of the blade from R241 to R878 with exceptions at the very front of the leading and the trailing edge. The suface-component of the bottom surface under flap bending loads are illustrated in figure 12.

The CAD description of the blade is superimposed on

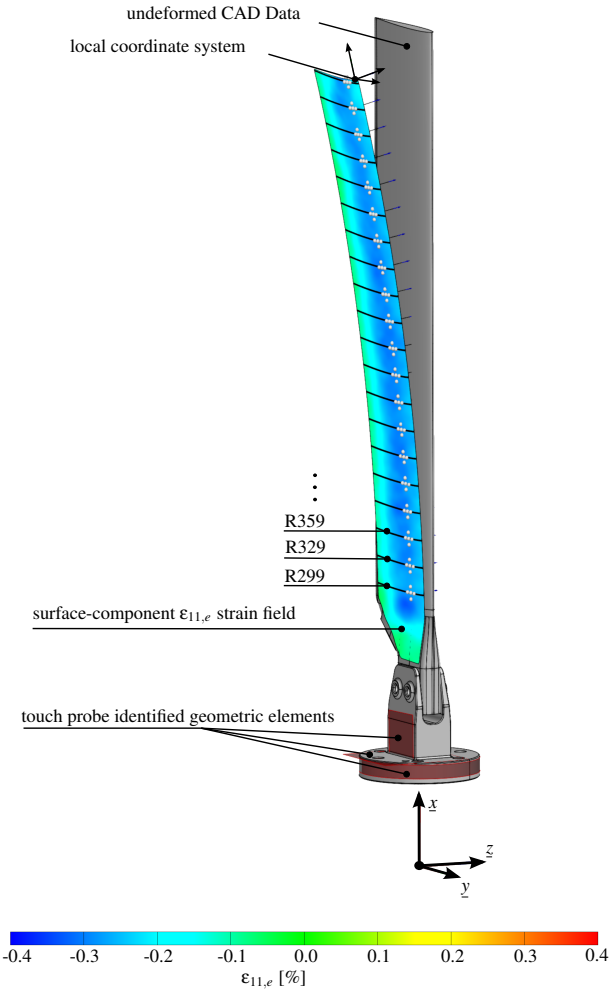

Fig. 12: postprocessing setup under load case L8.3 - Flap Bending, each radial section set combines a facet-point-component that is connected to a coordinate system at the beam axis.

the undeformed reference state within the software to align the coordinate system to the original target data using a best-fit. Figure 13 and table 4 show the top and bottom deviation of the surface-component versus the CAD data after the best fit was performed.

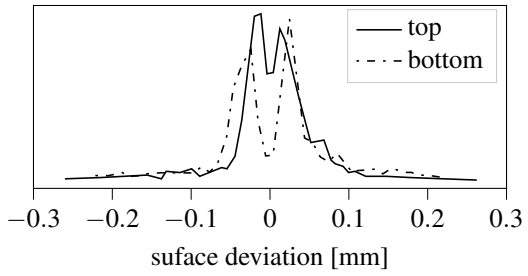

Fig. 13: reference surface deviation histogram of the best-fit surface-component versus the CAD

The very low surface deviation to the CAD design of the rotor blade indicates a precise machining and sanding of the molds, no distortion of the blade during curing, good

	surface deviation [mm]			
	mean	min	max	SD
top	0.016	-0.49	0.16	0.06
bottom	0.01	-0.19	0.20	0.05

Table 4: reference suface-component deviation

airfoil compliance along the span and a uniform paint and stochastic pattern application.

In order to obtain a better support of the individual punctual measured values for the strain tensor calculation, the software takes into account further neighboring points of radius 3 surrounding the point under consideration for the calculation.
Note that the strains are recovered in material, i.e. in local coordinates moving with the specimen. Therefore, each point has its own coordinate system. That is, the software calculates the strains of the sections in the moving coordinate systems $\mathcal{E}$ instead of the stationary global coordinate system. The $\underline{e}_3$-axis points in thickness direction. To ensure a common orientation, the software uses the normal of a local equalization plane around the point under consideration as the Z direction. The local $\underline{e}_1$-axis results from the cross product of the normal vector $\underline{n}_{LP}$ of the plane and the global X-axis. The local $\underline{e}_2$-axis then results from the cross product of the local $\underline{e}_3$-axis and the local $\underline{e}_1$-axis.

The measured strain field is split into multiple radial sections every 30 mm. To recover the deformed local coordinate system $\mathcal{C}$ of each section a facet-point-component with 5 facets of size 23 px is introduced as shown in figure 14. They are placed around 25% chord of the airfoil and sit right above the pitch and beam axis of the blade. The tagging function links the local coordinate system to a virtual center of gravity that is being calculated from the facet point component. This center of gravity describes the movement of the coordinate-system in space. Note that this local sectional coordinate system coincides with the local coordinate system of the deformed beam.

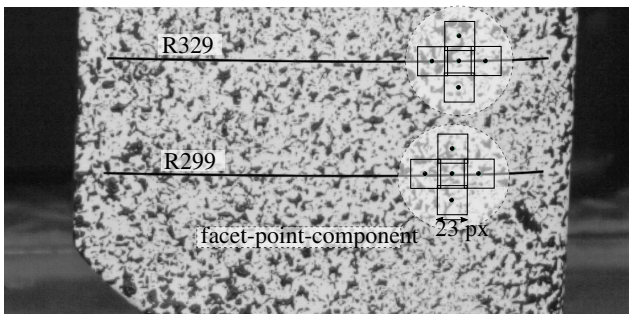

Fig. 14: facet-point-component definition on the bottom surface of the blade at R299 and R329 with a facet size of 23 x 23 px.

To obtain the sectional loads at each radial station the measured load and moment vectors of the load-cell are transformed according to the following relationship from

the global coordinate system $\mathcal{G}$ to the local sectional coordinate system $\mathcal{C}$. $\underline{p}^{(\mathcal{G})}$ is the position vector of the coordinate system and $\underline{\underline{A}}_{\mathcal{C}\mathcal{G}}$ is the transformation matrix containing the unit vectors of $\mathcal{C}$.

$$\underline{F}^{(\mathcal{C})} = \underline{\underline{A}}_{\mathcal{C}\mathcal{G}}\underline{F}^{(\mathcal{G})} \qquad (15)$$
$$\underline{M}^{(\mathcal{C})} = \underline{\underline{A}}_{\mathcal{C}\mathcal{G}}(-\underline{p}^{(\mathcal{G})} \times \underline{F}^{(\mathcal{G})} + \underline{M}^{(\mathcal{G})})$$

The hybrid approach of this method requires the experimental results to be mapped onto the finite element discretization by SONATA [11, 37]. Even tough the surface deviation compared to the CAD data is very low, small discrepancies are still noticeable when the experimental sections are transformed in local coordinates under deformation.
The surface-strains are mapped only onto the nearest nodal locations by linear interpolation. The partial derivatives of the calculated warping field are also recovered by linear interpolated derivatives over the mesh.

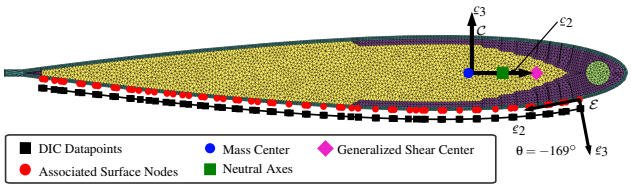

Fig. 15: finite element discretization of the homogeneous cross-section created by SONATA showing the maximum deviation of the measured nodal values at the R869 during torsion (L7.3)

Results

The stiffness matrix for the MERIT-A-001-2020-07 composite blade is examined in this section. The sectional stiffness properties are evaluated over the homogeneous region of the blade.
The axial surface strains ($\varepsilon_{11,e}$) are illustrated in figure 16 for the flap shear load case (U4-3). Under this load, the inevitable flap bending moment creates an axial strain distribution that has its sectional maximum at the maximum thickness location at 30% chord and decreases linearly along the span.

The axial surface strains ($\varepsilon_{11,e}$) are illustrated in figure 17 for pure flap bending (U9-3). Under this load, the flap bending moment creates a similar strain distribution with a sectional maximum at 30% chord but varies little over the homogeneous region along the span. The outermost radial section R869 already has additional plies within the layup to embed the balance cell within the structure. This leads to a decreased axial strain amplitude towards the tip. Similarly, the strain decreases towards the blade attachment as the sections becomes thicker and embed much more material. Figure 18 shows the top surface strain distribution ($\varepsilon_{11,e}$) under negative lag bending (U10.3, -Lag Bending).

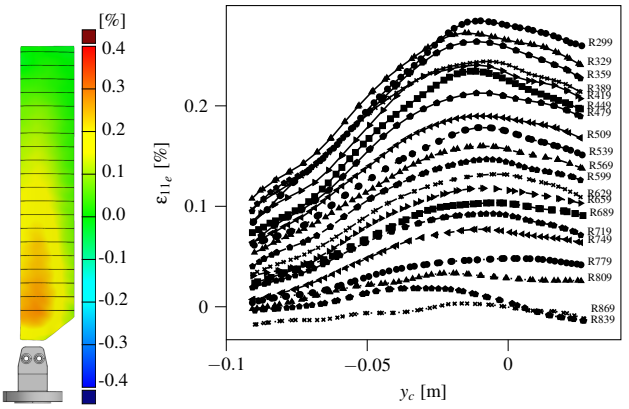

Fig. 16: DIC axial top surface strain distribution ($\varepsilon_{11,e}$) under positive flap shear (U4.3, +Flap Shear)

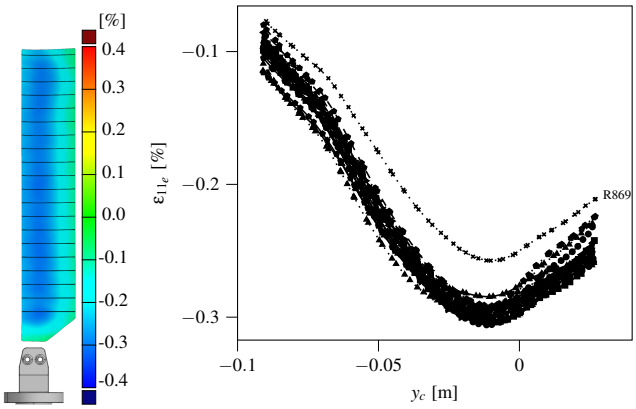

Fig. 17: DIC axial top surface strain distribution ($\varepsilon_{11,e}$) under positive flap bending (U9.3, +Flap Bending)

Comparable to the previous load case the sectional strain distribution varies little along the span apart from the outermost section and towards the blade attachment. The axial strain decreases chordwise towards the trailing edge.

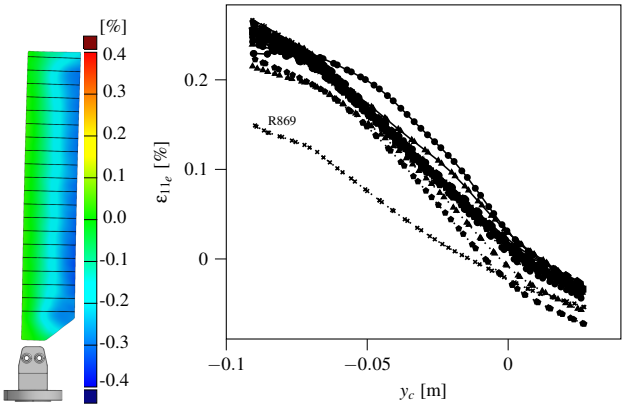

Fig. 18: DIC axial top surface strain distribution ($\varepsilon_{11,e}$) under negative lag bending (U10.3, -Lag Bending)

The section provides the results derived from the governing equations. For this study the examination of shear stiffness properties is neglected because differences of even an order of magnitude have an insignificant effect to the dy-

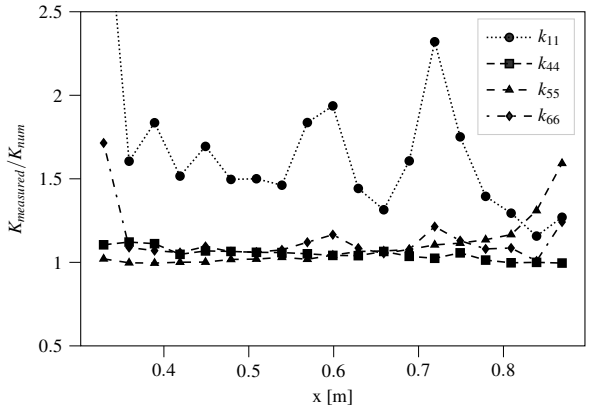

Fig. 19: variation of the stiffness properties along the span

namic response of rotor blades [1] but will be evaluated in future studies. Figure 19 shows the relative variation of the derived stiffness properties along the span of the rotor blade compared to the numerically predicted values. The torsional stiffness (k_{44}), flap bending stiffness (k_{55}), lead-lag bending stiffness (k_{66}) are all within a 10 to 15% range to the numerically predicted values. The increase of lead-lag and flap bending stiffness towards the tip of the blade is explained by the additional plies that begin to scarf towards a monolithic tip structure. The first section has an increased lead-lag stiffness as this was expected from the observed reduced axial strains of figure 18.

The axial stiffness k_{11} is overpredicted by an average of 60% with a large variation along the span. The load capacity of the test bench limited the maximum axial loads to 10kN which resulted in a poor signal to noise ratio.

However, note that the measured torsional stiffness k_{44} is on average 5% , the flap bending stiffness k_{55} 6.6% and the lead-lag bending stiffness 12 % higher than the predicted value of the numerical simulation.

Note that the material constitutive behavior, foundation of the numerical model, was determined experimentally prior to this study by a series of tensile tests [28]. Yet, uncertainties still exist because the manufacturing process of the blade is different to the test samples. Since the MERIT rotor blade has both a symmetric NACA0012 airfoil and a symmetric layup and no twist, the numerical simulation predicted many off-diagonal coupling relation terms to be very small or zero, which is why a relative comparison between the off-diagonal coupling relations is not possible. Table 5 summarizes the average stiffness properties together with the corresponding standard deviation (SD) while figure 20 shows the axial lead-lag coupling relation (k_{16}) which is also present in the numerical model yet has a large standard deviation. Again it is assumed, that the low signal to noise ratio is responsible for the large variation in axial coupling relations.

The bending and torsion coupling relations (k_{45}), (k_{46}) and (k_{56}) are all non-zero yet very small compared to their diagonal counterparts. Again, the increase towards the tip of the blade is caused by the changing layup.

	Measured	Numerical	SD
k_{11} [N]	6.08×10^7	3.54×10^7	1.71×10^7
k_{14} [Nm]	-476	0	4421
k_{15} [Nm]	-9720	-95.9	6509
k_{16} [Nm]	-5.56×10^5	-1.82×10^5	2.33×10^5
k_{44} [Nm^2]	766	727	24.4
k_{45} [Nm^2]	2.05	0	1.09
k_{46} [Nm^2]	-4.68	0	33.0
k_{55} [Nm^2]	856	803	61.9
k_{56} [Nm^2]	117	1.16	80.4
k_{66} [Nm^2]	23149	20581	3079

Table 5: average stiffness properties along the homogeneous region

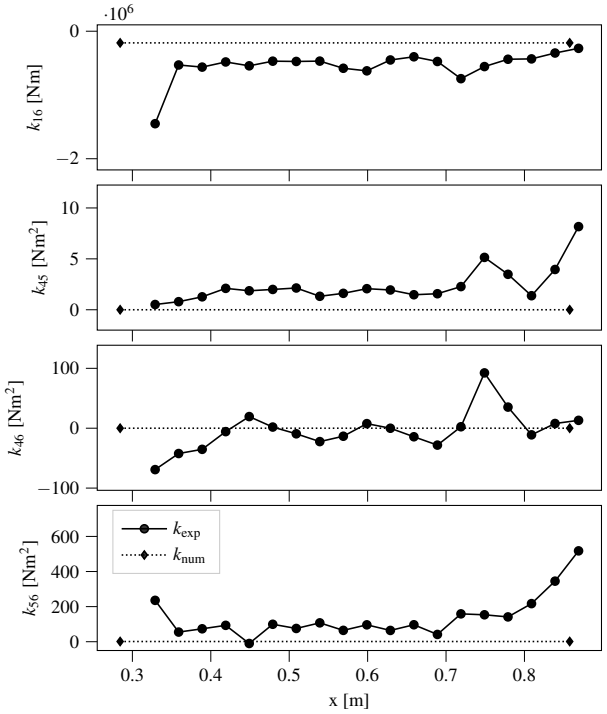

Fig. 20: variation of the off-diagonal stiffness properties along the span

Conclusions & Outlook

Following the novel hybrid approach by Sinotte and Bauchau [1], an experimental technique for the determination of the stiffness matrix has been presented. The hybrid method relies on the measurement of the strain field and combines it with a numerically determined warping field using SONATA and the cross-sectional analysis tool ANBA4 [12]. Digital Image Correlation was used to measure the surface strains on the top and bottom of the rotor blade under 6 independent load cases in positive and negative direction. The sectional loads were determined by measuring the loads using a 6-component load cell at the attachment.

The design and manufacturing of the MERIT rotor blades have been described in detail and served as test article for this study.

1. The coefficients along the diagonal of the stiffness matrix showed good agreement between the measured and predicted values by the numerical simulation. The measured torsional stiffness k_{44} is on average 5%, the flap bending stiffness k_{55} 6.6% and the lead-lag bending stiffness 12 % higher than the predicted value of the numerical simulation. With an coefficient of variation of 3%, 7% and 13% respectively.

2. The method is capable of capturing important coupling relations of the sectional stiffness matrix. Yet, this test article proved to be not particularly suitable to evaluate the performance of this method because of its symmetric design.

3. The axial stiffness coefficients showed large variations and deviations from its predicted values. Further experiments are planned to increase the axial load up to 40 kN with an improved cable routing in a universal testing machine to improve the signal to noise ratio.

4. Further plans are to extend the region of interest over the entire span of the blade. The region of particular interest is the transition region towards the blade attachment. Also, the uncertainty of the method shall be evaluated and compared to classical approaches.

5. Another future goal is to recover the warping field experimentally from the DIC displacement measurements.

Acknowledgment

Without the large assistance of Daniel Maraite of GOM, who supported us with an ARAMIS SRX sensor and its measurements this work would not have been possible. We would also like to thank the TUM Laboratory for Product Development and Lightweight Design, the TUM Chair of Carbon Composites and the TUM Workshop of the Physics Department for their generous support. Particular appreciation goes to Marco Morandini of Politecnico di Milano for the advice and support with ANBA4. This work was also assisted by Nils Roth [32] during his bachelor's thesis, in which he designed the balance scale and verified its performance and achievable measurement accuracy in various test series.

Copyright statement

REFERENCES

[1]Sinotte, T. and Bauchau, O. A., "Novel Approach for Experimental Measurement of Sectional Stiffness Properties of Composite Rotor Blades," *45th European Rotorcraft Forum, Warsaw, Poland*, 2019.

[2]Sinotte, T. and Bauchau, O. A., "Experimental Measurement of Sectional Stiffness Properties of Composite Rotor Blades," *Vertical Flight Society 76th Annual Forum*, 2020.

[3]Heuschneider, V., Berghammer, F., and Hajek, M., "Numerical and Experimental Study on the Modal Characteristics of a Rotor Test Rig," *Topics in Modal Analysis & Testing, Volume 8*, edited by B. Dilworth and M. Mains, Springer International Publishing, Cham, 2021, pp. 315–321.

[4]Heuschneider, V., Berghammer, F., Pflumm, T., and Hajek, M., "Development and Initial Hover Testing of the Mach Scaled Rotor Test Rig MERIT," *47th European Rotorcraft Forum, United Kingdom*, 2021.

[5]Johnson, W., "A History of Rotorcraft Comprehensive Analyses," *American Helicopter Society 60th Annual Forum, Baltimore, MD, June 7–10*, 2013.

[6]Bauchau, O. A., Bottasso, C. L., and Nikishkov, Y. G., "Modeling Rotorcraft Dynamics With Finite Element Multibody Procedures," *Mathematical and Computer Modelling*, Vol. 33, No. 10-11, 5 2001, pp. 1113–1137.

[7]Datta, A. and Johnson, W., "Three-Dimensional Finite Element Formulation and Scalable Domain Decomposition for High-Fidelity Rotor Dynamic Analysis," *Journal of the American Helicopter Society*, 2011.

[8]Cesnik, C. E. S. and Hodges, D. H., "VABS: A New Concept for Composite Rotor Blade Cross-Sectional Modeling," *American Helicopter Society 51st Annual Forum*, 1995.

[9]Han, S. and Bauchau, O. A., "Nonlinear three-dimensional beam theory for flexible multibody dynamics," *Multibody System Dynamics*, Vol. 34, No. 3, oct 2014, pp. 211–242.

[10]Bauchau, O. A. and Han, S., "Three-Dimensional Beam Theory for Flexible Multibody Dynamics," *Journal of Computational and Nonlinear Dynamics*, Vol. 9, No. 4, jul 2014.

[11]Feil, R., Pflumm, T., Bortolotti, P., and Morandini, M., "A Cross-sectional Aeroelastic Analysis and Structural Optimization Tool for Slender Composite Structures," *Composite Structures*, Vol. 253, dec 2020, pp. 112755.

[12]Morandini, M., Chierichetti, M., and Mantegazza, P., "Characteristic behavior of prismatic anisotropic beam via generalized eigenvectors," *International Journal of Solids and Structures*, Vol. 47, No. 10, may 2010, pp. 1327–1337.

[13]Yu, W., Volovoi, V., Hodges, D. H., and Hong, X., "Validation of the variational asymptotic beam sectional analysis," *AIAA Journal*, Vol. 40, No. 10, jan 2002, pp. 2105–2112.

[14]Rohl, P. J., Kumar, D., Dorman, P., Sutton, M., and Cesnik, C. E. S., "A Composite Rotor Blade Structural Design Environment for Aeromechanical Assessments in Conceptual and Preliminary Design," *American Helicopter Society 68th Annual Forum*, American Helicopter Society, 2012.

[15]Jung, S. N., You, Y. H., Lau, B. H., Johnson, W., and Lim, J. W., "Evaluation of Rotor Structural and Aerodynamic Loads Using Measured Blade Properties," *Journal of the American Helicopter Society*, Vol. 58, No. 4, Oct. 2013, pp. 1–12.

[16]Jung, S. N. and Lau, B. H., "Determination of HART I Blade Structural Properties by Laboratory Testing," Tech. Rep. NASA/CR–2012-216039, NASA, 2012.

[17]Onkar, A. K., Upadhyay, C. S., and Yadav, D., "Stochastic finite element buckling analysis of laminated plates with circular cutout under uniaxial compression," *Journal of applied mechanics*, Vol. 74, No. 4, 2007, pp. 798–809.

[18]Pflumm, T., Willem, Rex, and Hajek, M., "Propagation of Material and Manufacturing Uncertainties in Composite Helicopter Rotor Blades," *45th European Rotorcraft Forum, Warsaw, Poland*, 2019.

[19]Kuntze-Fechner, G., *Einführung in die Hubschraubertechnik*, Eurocopter Deutschland GmbH, 2004.

[20]Schürmann, H., *Konstruieren mit Faser-Kunststoff-Verbunden*, Springer, 2005.

[21]Vogl, J., *Konstruktive Auslegung eines 2-Blatt Heckrotorsystem für einen modernen Ultraleicht-Keinhubschrauber und Entwurf eines lagerlosen Heckrotorsystems*, Diploma thesis, Hochschule München, edm-aerotec GmbH, 2012.

[22]Mack, M. D., *Konstruktive Auslegung eines Hauptrotorblattes für einen modernen Ultraleicht-Kleinhubschrauber und Herstellung einer Prototypenkomponente*, Master's thesis, Hochschule München, edm-aerotec GmbH, 2011.

[23]Böhler Edelstahl GmbH & Co KG, *Technical Data Sheet - BÖHLER N352 Extra*, May 2018.

[24]SGL Carbon SE , *Product Data Sheet (PDS) - R*, May 2018.

[25]SGL Carbon SE , *Product Data Sheet (PDS) - SIGRAPREG® C W200 TW2/2 E503/45%*, May 2018.

[26]Pflumm, T., Barth, A., Kondak, K., and Hajek, M., "Auslegung und Konstruktion eines Hauptrotorblattes für ein in extremen Flughöhen operierendes Drehflügel-UAV," *Deutscher Luft- und Raumfahrtkongress, Rostock*, Rostock, 2015.

[27]Suesse, S. and Hajek, M., "Rotor Blade Displacement and Load Estimation with Fiber-Optical Sensors for a Future Health and Usage Monitoring System," *American Helicopter Society 74th Annual Forum*, 2018.

[28]Henschel, K. A., *Biocomposites in Aviation Structures on the Example of Flax and its Hybrids*, Dissertation, Technical University of Munich, München, 2019.

[29]AARONIA AG, *Technical Datasheet - Aaronia-Shield®, Rev 1.8-20.09.2016*, Sept. 2016.

[30]"Lochleibungsproben Programm 5, edm-aerotec GmbH„" 2013.

[31]Evonik, *Product Information - Rohacell® RIMA*, March 2020.

[32]Roth, N., *Konzept und Konstruktion einer Auswuchtvorrichtung für Rotorblätter des Experimentellen Rotorprüfstandes MERIT*, Bachelor's thesis, Technical University of Munich, 2020.

[33]Gaugelhofer, L., *Hybrid Experimental Measurement of Sectional Stiffness Properties of a Composite Rotor Blade with Digital Image Correlation*, mathesis, Technical University of Munich, Nov. 2020.

[34]Hajek, M., Manner, S., and Suesse, S., "Blade Root Integrated Fiber Bragg Grating Sensors-A Highly Redundant Data Source For Future HUMS," *Annual Forum Proceedings-AHS International*, 2015.

[35]ME-Meßsysteme GmbH, *Technical Datasheet - 6-Axis Force Sensor K6D130 5kN/500Nm/MP11*, May 2021.

[36]ME-Meßsysteme GmbH, *Calibration Certificate 20562699-1 - K6D130 5kN/500Nm SN:17402398*, Sept. 2020.

[37]Pflumm, T., Garre, W., and Hajek, M., "A Preprocessor for Parametric Composite Rotor Blade Cross-Sections," *44th European Rotorcraft Forum, Delft, The Netherlands*, September 2018.